

Turbulence measurements from compliant moorings - Part II: motion correction

Levi Kilcher*, Jim Thomson, Samuel Harding and Sven Nylund

**Corresponding author address: National Renewable Energy Laboratory, Golden, Colorado*

E-mail: Levi.Kilcher@nrel.gov

ABSTRACT

6 Acoustic Doppler velocimeters (ADV) are a valuable tool for making high-
7 precision measurements of turbulence, and moorings are a convenient and
8 ubiquitous platform for making many kinds of measurements in the ocean.
9 However—probably due to concerns that mooring motion can contaminate
10 turbulence measurements, and because acoustic Doppler profilers are rela-
11 tively easy to deploy—ADVs are not frequently deployed from moorings.
12 This work details a method for measuring turbulence using moored acoustic
13 Doppler velocimeters (ADVs) that corrects for mooring motion using mea-
14 surements from inertial motion sensors (IMUs). Three distinct mooring plat-
15 forms are deployed in a tidal channel with IMU-equipped ADVs. In each case
16 the inertial measurements dramatically reduce contamination from mooring
17 motion. The spectra from these measurements have a shape that is consistent
18 with other measurements in tidal channels, and have a $f^{-5/3}$ slope at high
19 frequencies—consistent with Kolmogorov’s theory of isotropic turbulence.
20 Motion correction also improves estimates of cross-spectra and Reynold’s
21 stresses. Comparison of turbulence dissipation with flow speed and turbulence
22 production indicates a bottom boundary layer production-dissipation balance
23 during ebb and flood that is consistent with the strong tidal forcing at the site.
24 These results indicate that IMU-equipped ADVs are a valuable new tool for
25 measuring turbulence from moorings.

26 1. Introduction

27 Acoustic Doppler velocimeters (ADV) have been used to make high-precision measurements
28 of water velocity for over 20 years (Kraus et al. 1994; Lohrmann et al. 1995). During that time they
29 have been deployed around the world to measure turbulence from a range of platforms, including:
30 stationary structures on ocean- and lake-bottoms, in surface waters from a pole lowered from
31 a ship’s bow, and in the deep ocean from autonomous underwater vehicles (e.g. Voulgaris and
32 Trowbridge 1998; Zhang et al. 2001; Kim et al. 2000; Goodman et al. 2006; Lorke 2007; Geyer
33 et al. 2008; Cartwright et al. 2009).

34 A relatively small fraction of ADV measurements have been made from moorings (e.g. Fer
35 and Paskyabi 2014). Presumably this is because mooring motion can contaminate ADV mea-
36 surements, and acoustic Doppler *profilers* (ADPs) can be used to measure mid-depth turbulence
37 statistics without a mooring (e.g. Stacey et al. 1999a; Rippeth et al. 2002; Wiles et al. 2006). Still,
38 ADV measurements have distinct characteristics that can be advantageous: they are capable of
39 higher sample-rates, they have higher signal-to-noise ratios, and they have a much smaller sample-
40 volume (1 centimeter, as opposed to several meters). That is, compared to an ADP, ADVs are high
41 precision instruments capable of providing unique information. They could be more widely used
42 as a moored-instrument (i.e. at arbitrary depth) if a method for accounting for mooring motion can
43 be demonstrated to provide more accurate estimates of turbulence statistics.

44 Inertial motion sensors (IMUs) have been used in the aerospace and aeronautical industries to
45 quantify the motion of a wide range of systems—including aircraft, rockets, and spacecraft—for
46 several decades, but their cost has come down as their market has grown beyond these niche sectors
47 (Bevly 2004). Over the last ten years massive growth in the smart-phone, drone, and ‘Internet
48 of Things’ markets has driven innovation in micro-electrical-mechanical systems (MEMS). One

49 component that has emerged from this sector is the IMU. Also known as ‘Magnetic, angular-rate,
50 gravity’ (MARG), or ‘attitude heading reference system’ (AHRS) sensors, IMUs measure three
51 axes of: the earth’s magnetic field, angular rotation, and linear acceleration. These signals are then
52 integrated using Kalman filters to estimate the orientation and motion of the sensor (Barshan and
53 Durrant-Whyte 1995; oáo Luis Marins et al. 2001; Bachmann et al. 2003)¹.

54 Nortek now offers a version of their Vector ADV with a Microstrain 3DM-GX3-25 IMU sen-
55 sor (Nortek 2005; MicroStrain 2012). The IMU’s signals are incorporated into the Vector data
56 stream so that the motion and orientation signals are tightly synchronized with the ADV’s velocity
57 measurements. This tight synchronization provides a data-stream that can be utilized to quan-
58 tify ADV motion in the earth’s inertial reference frame, and remove that motion from the ADV’s
59 velocity measurements at each time-step of its sampling. This work provides a detailed account-
60 ing for performing motion correction of these ‘ADV-IMU’ measurements, and presents results
61 of this method using data from a range of mooring configurations that positioned ADV-IMUs at
62 mid-depths in Puget Sound.

63 This effort was originally motivated by a need for low-cost, high-precision turbulence measure-
64 ments for the emerging tidal energy industry (McCaffrey et al. 2015; Alexander and Hamlington
65 2015). Experience in the wind energy industry has shown that wind turbine lifetime is reduced
66 by atmospheric turbulence, and the same is expected to be true for tidal energy turbines. In wind,
67 meteorological towers are often used to position sonic anemometers at the hub-height of wind
68 turbines for measuring detailed turbulence inflow statistics (Hand et al. 2003; Kelley et al. 2005;
69 Mücke et al. 2011; Afgan et al. 2013). In the ocean, tower-mounted hub-height turbulence mea-
70 surements have been made, but they are challenging to install and maintain in energetic tidal sites

¹Within this literature, ‘IMU’ is generally reserved for a MARG sensor without a magnetometer, but herein we refer to the entire group of sensors that measure motion using accelerometers and angular-rate sensors as ‘IMUs’.

71 (Gunawan et al. 2014). Thus, the Department of Energy funded this work to investigate the ac-
72 curacy of mooring deployed ADV-IMUs to reduce the cost of turbulence measurements at tidal
73 energy sites (Kilcher et al. 2016). The approach proved to be successful and potentially useful to
74 the broader oceanographic community interested in moored turbulence measurements (Lueck and
75 Huang 1999; Doherty et al. 1999; Nash et al. 2004; Moum and Nash 2009; Alford 2010; Paskyabi
76 and Fer 2013).

77 The next section describes details of the measurements, including a summary of the hardware
78 configurations (platforms) that were used to support and position the ADV-IMUs in the water-
79 column. A detailed description of the motion of these platforms is found in the companion paper to
80 this work, Harding et al. (2017), hereafter ‘Part 1’. Section 3 describes the mathematical details of
81 motion correction, and section 4 presents results from application of the method to measurements
82 from the various platforms. Section 5 is a discussion of the energetics of the tidal channel where the
83 measurements were made and demonstrates that the measurements are consistent with turbulence
84 theory and other measurement in similar regimes. A summary and concluding remarks is found in
85 section 6.

86 **2. Measurements**

87 This work is focused on measuring turbulence from ADVs that are deployed from non-stationary
88 platforms and equipped with inertial motion sensors (IMU). The ADVs utilized for these measure-
89 ments were all equipped with Microstrain 3DM-GX3-25 IMU sensors that captured all 6 compo-
90 nents of the ADV motion (3 components of angular rotation and 3 components of linear acceler-
91 ation), as well as the orientation of the ADV pressure-case. The sampling of the motion sensor is
92 tightly synchronized with the ADV measurements. The IMU measures its motion at 1kHz and uses
93 internal signal integration (Kalman filtering) to output the motion signals at the same sample rate

94 as the ADV's velocity measurements. This reduces aliasing of the IMU's motion measurements
95 above the ADV's sample-rate (MicroStrain 2010). Cable-head ADVs were utilized throughout
96 this work to allow for flexibility in the positioning of the ADV head relative to its pressure case.

97 All measurements used in this work were made in Admiralty Inlet, Washington, approximately
98 500 meters (m) WSW of Admiralty Head–Fort Casey State Park—in 60 m of water depth at latitude
99 48.153 north and longitude 122.687 west (Figure 1). The site is approximately 6 kilometers (km)
100 east of Port Townsend, and 1 km north of the Port Townsend – Coupeville ferry route. Admiralty
101 inlet is the largest waterway connecting Puget Sound to the Strait of Juan de Fuca, and it possesses
102 a large semi-diurnal tidal flow. This work utilizes data from three distinct deployment platforms:
103 the 'tidal turbulence mooring', a 'StableMoor' buoy, and a simple sounding weight. Additional
104 details, photos, and schematic diagrams of all three mooring systems can be found in Part 1.

105 *a. Tidal Turbulence Mooring (TTM)*

106 The 'tidal turbulence mooring' (TTM) is a simple mooring system with a 'strongback fin' sus-
107 pended between a steel clump-weight anchor weighing 1200 kilograms (kg) when dry and a 0.93
108 m-diameter spherical steel buoy with a buoyancy of 320 kg. The ADV pressure cases were
109 clamped to one side of the strongback fin and the ADV sensor head was positioned 10 cm in
110 front of the fin's leading edge (Figure 2). The leading edge of the fin is fastened inline with the
111 mooring line. This configuration was designed to work similar to a weather-vane, such that the
112 drag on the fin held the ADV head upstream of the mooring components. This work utilizes data
113 from two TTM deployments.

114 1) JUNE 2012 TTM DEPLOYMENT

115 The first was in June of 2012 at 48.15285 north, 122.68581 west. The mooring was in the water
116 from 17:30 on the 12th until 14:30 on the 14th (local, i.e. pacific daylight time). Two Nortek
117 ADVs were clamped to either side of the fin such that the axis of their cylindrical pressure-cases
118 were parallel with the leading edge of the strongback. The ADV heads were spaced 0.5 m apart
119 vertically along the fin. Only one of these ADVs was equipped with an integrated IMU. This TTM
120 also had an upward-looking acoustic Doppler profiler mounted on the mooring anchor.

121 Periods of time during which this mooring interfered with a beam of the Doppler profiler were
122 identified by inspection of the profiler's acoustic amplitude signal. Periods during which one
123 beam of the profiler had $> 5\%$ higher acoustic amplitude than the other beams were flagged as
124 'contaminated' and excluded from averaging. 5-minute averages in which more than 50% of the
125 data was contaminated in this way were masked as invalid.

126 2) JUNE 2014 TTM DEPLOYMENT

127 The second TTM deployment was in 2014 from 06:00 on June 17 to 05:00 on June 19 (local
128 time). The mooring was positioned at 48.15327 north, 122.68654 west. Two Nortek ADV-IMUs
129 were mounted on this TTM, with their heads spaced 0.5 m apart along the fin. In this case the
130 pressure-cases and ADV heads were inclined at an angle of 18° to the leading edge of the fin
131 to account for mooring blow-down during strong currents (Figure 3). This change was made
132 to reduce vibrational motion observed during the June 2012 deployment that was believed to be
133 associated with the orientation of the pressure cases.

134 *b. The StableMoor platform*

135 The second deployment platform was a cylindrical, ‘StableMoor’, syntactic foam buoy (man-
136 ufacturer: Deep Water Buoyancy) that was anchored to a clump weight that weighed 2700 lbs
137 (Figure 4). The buoy is 3.5 m long and 0.45 m in diameter with a tail ring that is 0.76 m in
138 diameter. The StableMoor weighs 295 kg in air, and has a buoyancy of 185 kg in water.

139 The StableMoor was ballasted to pitch upward a few degrees in zero-flow to avoid ‘flying down-
140 ward’. In the presence of an oncoming current the tail fins help to orient it into the flow. The
141 anchor for this buoy is similar to that of the TTM, including an acoustic release so the mooring
142 and anchor can be recovered separately.

143 The StableMoor platform has two primary advantages compared to the TTM. First, it is signif-
144 icantly more massive and hydro-dynamically stable than the TTM, which reduces the frequency
145 of motions of the platform. The other major advantage of the StableMoor platform is that it is
146 capable of supporting a bottom-tracking acoustic Doppler profiler, which provides an independent
147 measure of the platform’s translational motion. Disadvantages of the StableMoor include: a) its
148 size adds to the challenge of deployment and recovery, and b) it is significantly more expensive
149 than the TTM system.

150 This work uses data from two deployments of the StableMoor. During both deployments the
151 buoy was equipped with a 1200 kHz RDI workhorse sentinel acoustic Doppler profiler that was
152 oriented downward-looking to measure water velocity below the platform in 12 1-meter bins and
153 measure buoy motion (‘bottom tracking’), all at a 1 Hz sample rate.

154 1) ‘NOSE MODE’ STABLEMOOR DEPLOYMENT

155 The StableMoor was deployed with an ADV-IMU mounted at its nose from 11:21 on May 12 to
156 11:53 on May 13, 2015 (local time). This deployment was at 48.15277 north, 122.68623 west. In

157 this configuration the sample volume of the ADV, is 10 cm forward of the nose and 20 cm above the
158 centerline of the StableMoor (Figure 4, middle). Based on Wyngaard et al.'s (1985) investigation
159 of a similarly shaped slender body the velocity measurements should have flow-distortion effects
160 of less than 10%. This configuration was designed to be the most stable platform for measuring
161 turbulence from a moving platform.

162 2) 'WING MODE' STABLEMOOR DEPLOYMENT

163 The StableMoor buoy we used was customized to have an optional 1.5 m oval beam that holds
164 two ADVs 0.53 m to either side of the buoy hull (Figure 4, bottom). The StableMoor was deployed
165 in this configuration from 09:52 on May 11 to 06:23 on May 12, 2015 (local time). This configu-
166 ration provides a simultaneous measurement of turbulence at two points laterally to the oncoming
167 flow, which is a relatively unique mid-depth measurement.

168 *c. Turbulence Torpedo*

169 The turbulence torpedo is a simple sounding weight with an ADV head mounted forward of the
170 nose, and the ADV pressure case strapped below. This platform was deployed on May 14, 2015
171 for 37 minutes starting at 07:41 local time. This measurement was made from a davit that hung
172 the system from the side of the ship to a depth of approximately 25 m. The primary logistical
173 advantages of this platform are its compact size, low cost, and the flexibility to perform spatial
174 transects.

175 *d. Coordinate system and turbulence averaging*

176 Unless stated otherwise, vector quantities in this work are in a fixed 'principal-axes' coordinate
177 system that is aligned with the bi-directional tidal flow: positive u is in the direction of ebb (310°)

True), positive w is vertically upward, and v is the cross-stream component in a right-handed coordinate system. The full velocity vector, $\vec{u} = (\tilde{u}, \tilde{v}, \tilde{w})$, is separated into a mean and turbulent component as $\vec{u} = \bar{\vec{u}} + \vec{u}'$, where the over-bar denotes a 5 minute average. Turbulence kinetic energy, $\text{tke} = \overline{u'^2} + \overline{v'^2} + \overline{w'^2}$, and Reynold's stresses, $\overline{u'v'}$, $\overline{u'w'}$, $\overline{v'w'}$ are computed by averaging over the 5-minute window. Throughout this work we use $\bar{U} = (\bar{u}^2 + \bar{v}^2)^{1/2}$ to denote the mean horizontal velocity magnitude.

All spectra, $S\{x\}(f) = |\mathcal{F}\{x(t)\}|^2$, and cross-spectra, $C\{x,y\}(f) = \text{real}(\mathcal{F}\{x(t)\}\mathcal{F}\{y(t)\})$, are computed using NumPy fast Fourier transform routines (van der Walt et al. 2011). Here, $\mathcal{F}\{x(t)\}$ denotes the fast Fourier transform of a signal $x(t)$. Time series', e.g. $x(t)$, are linearly detrended and Hanning windowed prior to computing $\mathcal{F}\{x\}$ to reduce spectral reddening.

Throughout the remainder of this work the dependence of S and C on f is implied (e.g. $S\{x\}(f)$ is hereafter $S\{x\}$), and for other variables the dependence on t is implied. Spectra and cross-spectra are normalized to preserve variance: $\int S\{u\}df = \overline{u^2}$, and $\int C\{u,v\}df = \overline{uv}$. The notations $S\{\vec{u}\} = (S\{u\}, S\{v\}, S\{w\})$ and $C\{\vec{u}\} = (C\{u,v\}, C\{u,w\}, C\{v,w\})$ denote the set of spectra and cross-spectra for each velocity component and pairs of components, respectively.

Turbulence dissipation rates are computed as,

$$\varepsilon = \frac{1}{\bar{U}} \left(\alpha \left\langle (S\{u\} + S\{v\} + S\{w\}) f^{5/3} \right\rangle_{f_{IS}} \right)^{3/2} \quad (1)$$

Where $\alpha = 0.5$, and $\langle \rangle_{f_{IS}}$ denotes an average over the inertial-subrange of the velocity spectra and where the signal-to-noise ratio is small (Lumley and Terray 1983; Sreenivasan 1995). Throughout this work we take this average from 0.3 to 1 Hz for the u and v components, and 0.3 to 3 Hz for the w component.

3. Methodology

The essential approach of motion correction is to estimate time-series of velocity on a compliant mooring by obtaining an independent estimate of ADV head motion and removing that motion from the measured signal. Previous works have utilized inertial motion sensors to quantify the motion of ‘multi-scale profilers’ for the purpose of measuring the full spectrum of oceanic shear (Winkel et al. 1996). Nortek’s ADV-IMU measures the linear acceleration, \vec{a} , rotational-motion, $\vec{\omega}$, and orientation matrix, \mathbf{R} , of the ADV pressure case (body) in the earth reference frame. So long as the ADV head is rigidly connected to the ADV pressure case, it is possible to utilize the IMU motion signals to calculate the motion of the ADV head, and remove it from the measured velocity signal (Miller et al. 2008). The ADV head motion, is calculated as the sum of rotational and translational motion:

$$\begin{aligned}\vec{u}_h &= \vec{u}_\omega + \vec{u}_a + \vec{u}_{\text{low}} \\ &= \mathbf{R}^T \cdot \vec{\omega}^*(t) \times \vec{\ell}^* + \int \{\vec{a}(t)\}_{HP(f_a)} dt + \vec{u}_{\text{low}}\end{aligned}\tag{2}$$

Here ‘*’ superscripts denote quantities in the ADV’s local coordinate system, and $\vec{\ell}^*$ is the vector from the IMU to the ADV head. \mathbf{R}^T —the inverse of the orientation matrix—rotates vectors from the IMU to the earth reference frame. The notation $\{\vec{a}\}_{HP(f_a)}$ indicates that the IMU’s accelerometer signal is high-pass filtered (in the earth’s stationary reference frame) at a chosen filter-frequency, f_a . This is necessary because accelerometers have low-frequency noise, sometimes referred to as ‘bias-drift’ (Barshan and Durrant-Whyte 1995; Bevy 2004; Gulmammadov 2009).

Integrating \vec{a} to estimate \vec{u}_a amplifies the bias-drift noise at low-frequencies, which dramatically reduces the signal-to-noise ratio at those time scales (Figure A1). The high-pass filtering reduces this noise so that it does not contaminate motion correction, but real motion that exists at these frequencies is still lost in the low signal-to-noise ratio (Egeland 2014; VanZwieten et al. 2015).

219 This means that low-frequency motion is not well resolved by the IMU, and so there is a residual
 220 low-frequency translational motion, \vec{u}_{low} , that needs to be measured independently—or at the very
 221 least considered—when using motion corrected ADV-IMU data. The $\vec{\omega}$ and \vec{u}_{ω} estimates do not
 222 have the same issue because there is no integration involved, and because low-frequency bias-drift
 223 in the $\vec{\omega}$ sensors is stabilized by the IMU’s on-board Kalman filtering (i.e. the accelerometer and
 224 magnetometer signals provide estimates of down and North, respectively, which stabilize orienta-
 225 tion estimates and eliminates bias from rotation estimates).

226 The choice of high-pass filter for reducing low-frequency accelerometer noise depends on the
 227 flow conditions of the measurement, and the platform that is being used. In particular, filter-
 228 selection involves a trade off between filtering-out the bias-drift noise while not filtering-out
 229 measured motion that is unresolved by an independent measurement of \vec{u}_{low} . If an independent
 230 measure of low-frequency motion is available it can be used to increase the accuracy of \vec{u}_{h} at
 231 low-frequency. Note that, to avoid double counting, \vec{u}_{low} should be estimated by applying the
 232 complimentary low-pass filter to the independent measurement of low-frequency motion.

233 With this estimate of ADV head motion it is straightforward to correct the measured velocity,
 234 \vec{u}_{m} , to estimate the velocity in the earth’s inertial reference frame:

$$\vec{u}(t) = \vec{u}_{\text{m}}(t) + \vec{u}_{\text{h}}(t) \quad . \quad (3)$$

235 Note here that the ‘+’-sign is correct because head motion, \vec{u}_{h} , induces a measured velocity in the
 236 opposite direction of the head motion itself ($\vec{u}_{\text{m}} = \vec{u} - \vec{u}_{\text{h}}$).

237 For the TTM and Turbulence Torpedo we utilize $f_a = 0.0333\text{Hz}$ (30 second period), and assume
 238 that $\vec{u}_{\text{low}} = 0$. For the StableMoor $f_a = 0.2\text{Hz}$ (5 second period). The bottom-track velocity was
 239 low-pass filtered at this frequency to provide an estimate of \vec{u}_{low} , and \vec{a} was high-pass filtered at this
 240 frequency. We use 4-pole, bi-directional (zero-phase), Hanning filters for all filtering operations.

241 Additional details on motion correction—including a detailed accounting of the distinct co-
242 ordinate systems of the IMU, ADV pressure case, and ADV head—can be found in Kilcher
243 et al. (2016). Open-source Python tools for performing motion correction of ADV-IMU data—
244 including scripts that write processed data in Matlab and tabulated formats—are available at
245 <http://lkilcher.github.io/dolfyn/>.

246 4. Results

247 *a. Mean velocity*

248 Figure 7 shows a comparison of \vec{u} measured by an ADV-IMU mounted on a TTM, to that of
249 an upward-looking acoustic Doppler profiler mounted on the TTM anchor. This shows excellent
250 agreement between the ADV and Doppler profiler measurements of velocity. The \bar{u} , \bar{v} and \bar{w}
251 components have a root-mean-square error of 0.05, 0.13 and 0.03 m/s, respectively. While it
252 is important to note that there is some discrepancy between ADP and ADV measured velocities
253 (especially in \bar{v} , which is most likely due to incomplete motion correction), the agreement between
254 the magnitude and direction of these independent velocity measurements indicates that moored
255 ADV-IMUs provide a reliable estimate of velocity in the Earth’s reference frame.

256 *b. TTM spectra*

257 As discussed in detail in Part 1 the mooring motion of the TTM, $S\{\vec{u}_h\}$, has a peak at 0.1 to 0.2
258 Hz from swaying of the mooring that is most likely driven by eddy-shedding from the spherical
259 buoy (Figure 8, red lines). There is also higher-frequency broad-band motion that is associated
260 with fluttering of the strongback fin around the mooring line. Both of these motions are especially
261 energetic in the v -component spectra, because this is the direction in which the TTM mooring

262 system is most unstable. As is expected from fluid-structure interaction theory the amplitude of
263 these motions increases with increasing mean velocity (Morison et al. 1950).

264 The mooring motion contaminates the uncorrected ADV-measurements of velocity, $S\{\vec{u}_m\}$,
265 whenever the amplitude of the motion is similar to or greater than the amplitude of the turbulence.
266 Fortunately, much of this motion can be removed using the IMU’s motion signals as detailed in
267 section 3. Lacking an independent measurement of turbulence velocity at this site, we interpret the
268 agreement of these spectra with turbulence theory and as evidence of the success of the method.
269 In particular, at high-frequencies ($f > 0.3$ Hz) for each mean-flow speed the spectra decay with
270 a $f^{-5/3}$ slope and have equal amplitude across the velocity components. These results are con-
271 sistent with Kolmogorov’s (1941) theory of isotropic turbulence, and are consistent with spectral
272 shapes of earlier measurements of turbulence in energetic tidal channels from stationary platforms
273 (Kolmogorov 1941; Walter et al. 2011; Thomson et al. 2012; McMillan et al. 2016).

274 For $|\vec{u}| > 1.0$, motion correction modifies the u and v component spectra at frequencies as high
275 as 3Hz. This indicates that in order for motion correction to be effective, synchronization between
276 the ADV and IMU needs to be within 1/3 second or better. This suggests that asynchronous
277 approaches to motion correction may be challenging, especially considering that the clock-drift of
278 some instrumentation can be as high as a few seconds per day. By integrating the IMU data into
279 the ADV data stream, the Nortek IMU-ADV achieves a synchronization to within 1e-2 seconds.

280 At low frequencies, the spectra tend to become roughly constant (especially at higher flow
281 speeds), which is also consistent with previous works. Note here, that the very-low magnitude
282 of $S\{\vec{u}_h\}$ at low frequencies is partially a result of filtering the IMU’s accelerometer signal when
283 calculating \vec{u}_a . The true low-frequency spectrum of ADV-head motion is unknown (indicated us-
284 ing a dashed line below f_a). A comparison of $S\{\vec{u}\}$ measured by the TTM to that measured by
285 the ADP—during the June 2012 deployment—are in agreement at low-frequencies (not shown).

286 This suggests that the assumption that $\vec{u}_{\text{low}} = 0$ at these frequencies, at this site, for this platform
287 is justified—even if $S\{\vec{u}_h\}$ is not as low as indicated in Figure 8.

288 As successful as motion correction is, some of the motion contamination persists in $S\{\vec{u}\}$. This
289 is most notable in $S\{v\}$ at the highest flow speeds (> 2.0 m/s): a peak at 0.15 Hz is an order of
290 magnitude larger than a spectral fit to the other frequencies would indicate. This persistent motion
291 contamination is evident to a lesser degree in $S\{u\}$ for $|u| > 2$ m/s, and in $S\{v\}$ at lower flow
292 speeds. $S\{w\}$ appears to have no persistent motion contamination because the amplitude of the
293 motion in this direction is much lower than for the other two components. For these measurements,
294 $S\{w_h\}$ is so low that w -component motion correction is only necessary when $|u| > 2$ m/s.

295 The amplitude of the persistent motion contamination peaks in $S\{v\}$ at 0.15 Hz are a factor of 5 to
296 10 times smaller than the amplitude of the ADV head motion itself. This suggests the Microstrain
297 IMU can be used to effectively correct for mooring motion at 0.15 Hz when the amplitude of that
298 motion is less than 3 times the amplitude of the real turbulence spectrum. Where we have chosen
299 a value of 3 as a conservative estimate of motion correction’s effectiveness.

300 This reveals an ancillary benefit of the IMU measurements: in addition to the primary benefit of
301 correcting for mooring motion, they can also be used to identify and screen-out persistent motion
302 contamination. For example, one of the most common uses of turbulence spectra is for the calcu-
303 lation of ϵ and tke . For these purposes, based on the relative amplitudes of the 0.15 Hz peaks, we
304 assume that persistent motion contamination is likely where $S\{\vec{u}_h\}/S\{\vec{u}\} > 3$ and exclude these
305 regions from spectral fits.

306 In the present case, for the u and w spectra, this criteria only excludes a narrow range of frequen-
307 cies at the 0.15 Hz motion peak for some cases. This criteria is more restrictive of the v -component
308 spectra at high frequencies for $\bar{U} > 1.0$ m/s, but this may be acceptable because the amplitude of

the spectrum at these frequencies—i.e. in the isotropic inertial subrange—should be equal to that of u and w (Kolmogorov 1941).

Agreement of the v -component spectral amplitude with that of u and w at frequencies > 0.3 Hz indicates that motion correction is effective at those frequencies even when $S\{\vec{u}_h\}/S\{\vec{u}\} > 3$. This suggests that our screening threshold is excessively conservative at those frequencies, and that a more precise screening threshold is frequency dependent. For example, it might take into account the f^3 character of the noise in $S\{\vec{u}_a\}$ (Figure A1). For the purposes of this work the $S\{\vec{u}_h\}/S\{\vec{u}\} < 3$ threshold for spectral fits is sufficient, and detailed characterization of the IMU’s motion- and frequency-dependent noise level is left for future work.

c. StableMoor Spectra

The spectra of the stablemoor motion has a broader peak with a maximum amplitude that is approximately half the frequency of the TTM spectral peak (Figure 9). The motion of this platform also does not have high-frequency ‘sub-peaks’ or other high-frequency broad-banded excitation (Part 1). These characteristics of the motion are most-likely due to the more massive and hydro-dynamically streamlined properties of the platform.

Like the TTM, the motion-corrected spectra from the StableMoor are consistent with turbulence theory and previous observations. Most importantly, there is an improvement in the quality of the motion corrected spectra compared to the TTM. In particular the persistent motion contamination peaks appear to be completely removed. That is, this measurement system provides an accurate estimate of the turbulence spectra at this location from low frequencies to more than 1 Hz—well into the inertial sub-range—for all three components of velocity.

Note that this level of accuracy can not be obtained without the independent estimate of \vec{u}_{low} . If we assume that $\vec{u}_{low} = 0$ a similar plot to Figure 9 (not shown) reveals persistent motion-

contamination peaks and troughs in the u - and v -spectra regardless of the choice of f_a . This indicates that the low-frequency motion of the StableMoor is below a threshold where the IMU's signal to noise ratio is high enough to resolve its motion. In other words, compared to the TTM, the StableMoor platform provides a more accurate measurement of turbulence when it includes an independent measure of \vec{u}_{low} (here a bottom-tracking ADCP), but it does no better—and perhaps worse—when it doesn't.

d. Torpedo spectra

The u and v motion of the turbulence 'torpedo' is broad-banded and the w motion has a narrow peak at 0.3 Hz (Figure 10). Because \vec{u}_h is estimated using $f_a = 0.0333Hz$ and assuming $\vec{u}_{low} = 0$ its spectra rolls-off quickly below f_a . A better estimate of \vec{u}_{low} could be obtained by accounting for ship motion, but this has not been done here.

Motion correction of the torpedo data appears to effectively remove a motion from $S\{w\}$ at 0.3Hz, and straightens out $S\{v\}$ between 0.04 and 0.6Hz. $S\{u\}$ is relatively unimproved by motion correction, apparently because the torpedo motion is smaller than the turbulence in this direction. At frequencies below f_a , $S\{u\}$ and $S\{v\}$ increase dramatically. This suggests that unresolved low-frequency motion of the torpedo is contaminating the velocity measurements at these frequencies. It may be possible to correct for some of this using a measurement of the ship's motion as a proxy for the torpedo's low-frequency motion, but this has not been done. Still, above f_a , the torpedo appears to provide a reliable estimate of spectral amplitude in the inertial subrange and can therefore be used to estimate ε . Considering the simplicity of the platform it may be a useful option for quantifying this essential turbulence quantity in a variety of scenarios. If a GPS is positioned above it, it may be capable of providing even more.

354 *e. Cross-spectra*

355 Inspection of cross-spectra from TTM measurements demonstrates that motion correction can
356 reduce motion contamination to produce reliable estimates of velocity cross-spectra (Figure 11).
357 At low flow speeds (left column), cross-spectra between components of \vec{u}_h (i.e. between compo-
358 nents of head-motion, red) are small compared to correlated velocities. As the velocity magnitude
359 increases (center, and right columns), the swaying motion of the TTM at 0.15 Hz appears as a
360 peak in the amplitude of the cross-spectra of \vec{u}_h and \vec{u}_m (black) for all three components of cross-
361 spectra (rows). Fortunately, motion correction reduces the amplitude of this peak dramatically so
362 that $C\{\vec{u}\}$ (blue) is small at 0.15 Hz compared to lower frequencies. Furthermore, the fact that the
363 standard deviation of $C\{\vec{u}\}$ is also relatively small at 0.15 Hz suggests that motion correction is
364 effective for each spectral window, not just in their mean.

365 These results indicate that motion-corrected TTM velocity measurements can be used to obtain
366 reliable estimates of turbulence Reynold's stresses, which are the integral of the cross-spectra.
367 Without motion correction, Reynold's stress estimates would be contaminated by the large peaks
368 in the cross-spectra that are due to the swaying and fluttering motion of the TTM vane.

369 A similar investigation of StableMoor cross-spectra (not shown) indicates that cross-spectral
370 motion contamination is much lower amplitude than for the TTM. The low-frequency (< 0.3
371 Hz) 'swimming' motion of that platform produces minimal cross-spectral signal, and the relative
372 large-mass of the platform minimizes the kinds of higher-frequency swaying/fluttering that creates
373 large values of cross-spectral head-motion. Thus, the StableMoor platform also produces reliable
374 estimates of Reynold's stresses, which are presumed to be improved by motion correction.

5. Discussion

The beginning of the previous section presented a comparison of \vec{u} measured by a TTM-mounted ADV, to measurements from a co-located ADP. This demonstrated that the IMU provides a reliable estimate of the ADV's orientation and that this can be utilized to estimate mean velocity in the earth's reference frame. Turbulence velocity estimates from the same ADP are also in agreement with low-frequency TTM turbulence estimates (not shown), but the ADP does not resolve turbulence at the scales where motion contamination is strongest (0.1 to 1.0 Hz).

Ideally, moored motion-corrected turbulence velocity measurements would be validated against simultaneous independent validated measurements of turbulence velocity at the same scales, exact time and exact location. Accomplishing this, however, involves significant technical challenges not easily overcome—most notably the difficulty of measuring turbulence at the same point as the moving ADV. A slightly less ideal but much more realistic confirmation of the methodology might involve comparing the statistics of moored turbulence measurements to that from a nearby fixed platform, or a fixed platform placed at the same location at a different time (e.g. the 'TTT' platform described in Thomson et al. 2012). Unfortunately, to our knowledge, these measurements have not yet been made.

Lacking a relevant, fixed, independent turbulence measurement to compare to it is instructive to demonstrate the degree to which the moored measurements are consistent with turbulence theory and other turbulence measurements in similar flow environments. The previous section showed that the shape of the turbulence velocity spectra from moored ADVs is consistent with Kolmogorov's theory of locally isotropic turbulence, which has been observed consistently in turbulence measurements for decades (Kolmogorov 1941; Grant et al. 1962; McMillan et al. 2016). In particular, we observed an isotropic subrange—an $f^{-5/3}$ spectral slope, and equal amplitude

spectra between components—that is driven by anisotropic turbulence at longer time-scales (Figures 8, 9, 10). This is interpreted as the first indication that the measurement systems presented are capable of accurately resolving turbulence. The degree to which uncorrected spectra were corrected toward this theoretical and observationally confirmed shape is interpreted as a measure of the improvement of the spectral estimates by motion correction.

Figure 12 presents a time-series of the mean velocity (A) and several turbulence statistics that were measured during the June 2014 TTM deployment. This figure shows the evolution of the flow through Admiralty Inlet during 1.5 tidal cycles. The tke (B), Reynold’s stresses (C), dissipation and one component of turbulence production (D) grow and strengthen with ebb or flood, then subside during slack tide. This component of turbulence production is:

$$P_{uz} = \frac{\partial \bar{u}}{\partial z} \overline{uw} \quad . \quad (4)$$

Where $\partial \bar{u} / \partial z$ is computed from the two ADV’s on the TTM. The highest values of ε and P_{uz} occur at the peak of the ebb or flood, which is in agreement with other measurements in tidal channels. The agreement of the magnitude of P_{uz} with ε at those times suggests a local production-dissipation balance that is often observed in tidally forced channels (Trowbridge et al. 1999; Stacey et al. 1999b; McMillan et al. 2016). At other times the value of P_{uz} is insufficient to balance ε or is negative.

Inspection of the negative P_{uz} values reveals that most of them are due to a reversed sign of \overline{uw} rather than a reversed sign of $\partial u / \partial z$ (i.e. when compared to the sign of u). This suggests that uncertainty in \overline{uw} may be contributing to discrepancies between P_{uz} and ε . Furthermore, considering the complex nature of the shoreline near this site (i.e. the headland), it is unsurprising that P_{uz} does not balance ε perfectly. Other terms of the tke equation are likely to be important, such as other components of production, advection terms, or turbulent transport terms. The fact

that these two terms are in near-balance as often as they are is a strong indication that bottom boundary layer physics are an important piece of the dynamics at this site.

Figure 13 compares individual values of $P_{u\bar{z}}$ with ε directly. Given the assumptions implicit in this comparison, and the discussion above, the agreement between $P_{u\bar{z}}$ and ε is an encouraging result that suggests the turbulent boundary reaches the depth of these measurements (10 m) during the highest flow speeds. This result is further supported by a comparison of \bar{U} with ε (Figure 14). Here we see a $\varepsilon \propto \bar{U}^3$ dependence that is again suggestive of bottom boundary layer physics (Trowbridge 1992; Nash et al. 2009). At lower flow speeds, ε deviates from this relationship, which suggests that the boundary layer is no longer the dominant physical process at the depth of these measurements.

6. Conclusion

This work presents a methodology for measuring turbulence from moored IMU-ADV, and details an approach for removing the IMU-measured mooring motion from the ADV's velocity measurements. The IMU integrated into the Nortek Vector ADV has been configured to provide estimates of the ADV's orientation and motion at every time-step of the ADV's sampling. The tight integration of the IMU and ADV data streams provides a data set that can be used to correct velocity measurements for mooring motion and rotate those measurements into the earth's reference frame.

Comparison of spectra of ADV head motion, $S\{\vec{u}_h\}$, to that of motion-corrected, $S\{\vec{u}\}$, and uncorrected spectra, $S\{\vec{u}_m\}$, reveals that motion correction improves spectral estimates of moored ADV measurements. In particular, we find motion corrected spectra have spectral shapes that are similar to previous measurements of tidal-channel turbulence and have a $f^{-5/3}$ spectral slope at

442 high frequencies. This suggests that the motion-corrected spectra resolve the inertial subrange
443 predicted by Kolmogorov’s theory of locally isotropic turbulence.

444 Motion correction reduces motion contamination for all platforms we presented, but it does not
445 necessarily remove it completely. This seems to depend on the relative amplitude of platform
446 motion compared to the underlying turbulence being measured. The most notable example of this
447 is from the TTM, which has a large ‘swaying’ peak at 0.1 Hz. Where this peak is very large—
448 especially in the v -component—it is not reduced to a level that is consistent with earlier mea-
449 surements of tidal-channel turbulence—i.e. there is no ‘smooth roll-off’ between low-frequency
450 energy-containing scales and the $f^{-5/3}$ inertial subrange.

451 This inconsistency indicates that turbulence measurements from moored, motion-corrected
452 IMU-ADVs must be interpreted with care. An inspection of spectra presented here suggests
453 that excluding spectral regions where $S\{\vec{u}_h\}/S\{\vec{u}\} > 3$ removes ‘persistent motion contamina-
454 tion’ peaks, while still preserving spectral regions where motion correction is effective. Using this
455 criteria it is then possible to produce spectral fits that exclude persistent motion contamination,
456 and provide reliable estimates of turbulence quantities of interest (e.g. ε and tke).

457 We also find that motion correction reduces motion contamination in cross-spectra. This is im-
458 portant because it suggests that moored IMU-ADV measurements may be used to produce reliable
459 estimates of Reynolds stresses. We utilized these stress estimates and vertical shear estimates,
460 both from the TTM, to estimate P_{uz} .

461 Finally, we’ve shown that ε estimates based on motion-corrected spectra scale with the U^3 , and
462 balance P_{uz} estimates during ebb and flood. Together, these results indicate that bottom boundary
463 layer physics are a dominant process at this site, and that the boundary layer reaches the height of
464 the IMU-ADVs (10 m) during ebb and flood. The degree of agreement between P_{uz} and ε also
465 serves as an indicator of the self-consistency of moored IMU-ADV turbulence measurements.

466 *Acknowledgments.* Many thanks to Joe Talbert, Alex DeKlerk, Captain Andy Reay-Ellers, Jen-
467 nifer Rinker, and Maricarmen Guerra in assisting with data collection. The authors are also grateful
468 to James VanZwieten, Matthew Egeland and Marshall Richmond for discussion on the details of
469 this work.

A1. Comparing StableMoor \vec{u}_{low} to IMU \vec{u}_{h}

In order to better understand the IMU's signal-to-noise ratio, it is instructive to compare the motion of the StableMoor buoy from the ADP bottom track measurements, u_{BT} , to the IMU's estimates of ADP motion. To do this, we compute the IMU's estimate of ADP motion using equation (2), and replacing ℓ^* with the vector that points from the IMU to the ADP head. We then linearly interpolated the ADP measurements onto the times of the ADV-IMU measurements.

The coherence between these two signals is high and statistically significant over 1.5 decades (from 0.03 to 0.8 Hz). The v component has the highest coherence, 98%, because this is the direction that has the most motion and therefore these estimates have a higher signal to noise ratio. The u and w components have slightly lower coherence, 80% and 65%, respectively, which indicates the *convolved* signal to noise ratio of these measurements.

On the low-frequency side, our interpretation is that the signal to noise ratio of the IMU increases dramatically below 0.03 Hz, resulting in low coherence. On the high-frequency side Doppler-noise in the ADP measurements contaminates its estimates of motion, causing the decrease in coherence at 0.8 Hz. A comparison of the phase between these signals shows that there is no lag between the measurements (not shown).

These results help to inform the selection of zero-lag filters used to estimate \vec{u}_{low} from u_{BT} . In particular, by selecting 0.2 Hz, we target the middle of the coherence peak between the two measurements. Furthermore, the rapid decrease in coherence below 0.03 Hz provides an objective measure of the performance of the frequency at which IMU measured velocity becomes unreliable in the flow conditions we observed.

References

- Afgan, I., J. McNaughton, S. Rolfo, D. Apsley, T. Stallard, and P. Stansby, 2013: Turbulent flow and loading on a tidal stream turbine by les and rans. *International Journal of Heat and Fluid Flow*, **43**, 96–108.
- Alexander, S. R., and P. E. Hamlington, 2015: Analysis of turbulent bending moments in tidal current boundary layers. *Journal of Renewable and Sustainable Energy*, **7** (6), 063 118.
- Alford, M. H., 2010: Sustained, full-water-column observations of internal waves and mixing near mendocino escarpment. *Journal of Physical Oceanography*, **40** (12), 2643–2660, doi: 10.1175/2010JPO4502.1, URL <http://dx.doi.org/10.1175/2010JPO4502.1>, <http://dx.doi.org/10.1175/2010JPO4502.1>.
- Bachmann, E. R., X. Yun, D. McKinney, R. B. McGhee, and M. J. Zyda, 2003: Design and implementation of MARG sensors for 3-DOF orientation measurement of rigid bodies. *International Conference on Robotics & Automation*, Taipei, Taiwan.
- Barshan, B., and H. F. Durrant-Whyte, 1995: Inertial navigation systems for mobile robots. *IEEE Transactions on Robotics and Automation*, **11** (3), 328–342.
- Bevly, D. M., 2004: Global positioning system (gps): A low-cost velocity sensor for correcting inertial sensor errors on ground vehicles. *Journal of dynamic systems, measurement, and control*, **126** (2), 255–264.
- Cartwright, G. M., C. T. Friedrichs, P. J. Dickhudt, T. Gass, and F. H. Farmer, 2009: Using the acoustic doppler velocimeter (adv) in the mudbed real-time observing system. *Marine Technology for Our Future: Global and Local Challenges*.

513 Doherty, K., D. Frye, S. Liberatore, and J. Toole, 1999: A moored profiling instrument*. *Journal*
514 *of Atmospheric and Oceanic Technology*, **16** (11), 1816–1829.

515 Egeland, M. N., 2014: Spectral evaluation of motion compensated ADV systems for ocean turbu-
516 lence measurements. Ph.D. thesis, Florida Atlantic University.

517 Fer, I., and M. B. Paskyabi, 2014: Autonomous ocean turbulence measurements using shear probes
518 on a moored instrument. *Journal of Atmospheric and Oceanic Technology*, **31** (2), 474–490, doi:
519 10.1175/JTECH-D-13-00096.1, URL <http://dx.doi.org/10.1175/JTECH-D-13-00096.1>, [http://](http://dx.doi.org/10.1175/JTECH-D-13-00096.1)
520 dx.doi.org/10.1175/JTECH-D-13-00096.1.

521 Geyer, R. W., M. E. Scully, and D. K. Ralston, 2008: Quantifying vertical mixing in estuaries.
522 *Environmental Fluid Mechanics*, **8**, 495–509, doi:10.1007/s10652-008-9107-2.

523 Goodman, L., E. R. Levine, and R. G. Lueck, 2006: On measuring the terms of the turbulent
524 kinetic energy budget from an auv. *Journal of Atmospheric and Oceanic Technology*, **23** (7),
525 977–990, doi:10.1175/JTECH1889.1, URL <http://dx.doi.org/10.1175/JTECH1889.1>, [http://dx.](http://dx.doi.org/10.1175/JTECH1889.1)
526 [doi.org/10.1175/JTECH1889.1](http://dx.doi.org/10.1175/JTECH1889.1).

527 Grant, H. L., R. W. Stewart, and A. Moilliet, 1962: Turbulence spectra from a tidal channel.
528 *Journal of Fluid Mechanics*, **12**, 241–263.

529 Gulmammadov, F., 2009: Analysis, modeling and compensation of bias drift in mems inertial
530 sensors. *Recent Advances in Space Technologies, 2009. RAST'09. 4th International Conference*
531 *on*, IEEE, 591–596.

532 Gunawan, B., V. S. Neary, and J. Colby, 2014: Tidal energy site resource assessment in the East
533 River tidal strait, near Roosevelt Island, New York, NY (USA). *Renewable Energy*, **71**, 509–
534 517, doi:10.1016/j.renene.2014.06.002.

535 Hand, M. M., N. D. Kelley, and M. J. Balas, 2003: Identification of wind turbine response to
 536 turbulent inflow structures. Tech. Rep. NREL/CP-500-33465, National Renewable Energy Lab-
 537 oratory.

538 Harding, S., L. Kilcher, and J. Thomson, 2017: Turbulence measurements from compliant moor-
 539 ings - part 1: Motion characterization, in review.

540 Kelley, N. D., B. J. Jonkman, G. N. Scott, J. T. Bialasiewicz, and L. S. Redmond, 2005: The impact
 541 of coherent turbulence on wind turbine aeroelastic response and its simulation. *WindPower*,
 542 Denver, Colorado, NREL/CP-500-38074, may 15-18.

543 Kilcher, L., J. Thomson, J. Talbert, and A. DeKlerk, 2016: Measuring turbulence from moored
 544 acoustic Doppler velocimeters: A manual to quantifying inflow at tidal energy sites. Tech. Rep.
 545 62979, National Renewable Energy Laboratory. URL www.nrel.gov/docs/fy16osti/62979.pdf.

546 Kim, S. C., C. T. Friedrichs, J. P.-Y. Maa, and L. D. Wright, 2000: Estimating bottom stress in
 547 tidal boundary layer from acoustic doppler velocimeter data. *Journal of Hydraulic Engineering*,
 548 399–406.

549 Kolmogorov, A. N., 1941: Dissipation of energy in the locally isotropic turbulence. *Dokl. Akad.*
 550 *Nauk SSSR*, **32** (1), 16–18, URL <http://www.jstor.org/stable/51981>.

551 Kraus, C., A. Lohrmann, and R. Cabrera, 1994: A new acoustic meter for measuring 3d laboratory
 552 flows. *Journal of Hydraulic Engineering*, **120**, 406–412.

553 Lohrmann, A., R. Cabrera, G. Gelfenbaum, and J. Haines, 1995: Direct measurements of reynolds
 554 stress with an acoustic doppler velocimeter. *Current Measurement, 1995., Proceedings of the*
 555 *IEEE Fifth Working Conference on*, 205–210, doi:10.1109/CCM.1995.516175.

556 Lorke, A., 2007: Boundary mixing in the thermocline of a large lake. *Journal of Geophysical*
557 *Research: Oceans*, **112** (C9), n/a–n/a, doi:10.1029/2006JC004008, URL [http://dx.doi.org/10.](http://dx.doi.org/10.1029/2006JC004008)
558 [1029/2006JC004008](http://dx.doi.org/10.1029/2006JC004008), c09019.

559 Lueck, R. G., and D. Huang, 1999: Dissipation measurement with a moored instrument in a swift
560 tidal channel. *Journal of atmospheric and oceanic technology*, **16**, 1499–1505.

561 Lumley, J., and E. Terray, 1983: Kinematics of turbulence convected by a random wave field.
562 *Journal of Physical Oceanography*, **13** (11), 2000–2007.

563 McCaffrey, K., B. Fox-Kemper, P. E. Hamlington, and J. Thomson, 2015: Characterization of
564 turbulence anisotropy, coherence, and intermittency at a prospective tidal energy site: Observa-
565 tional data analysis. *Renewable Energy*, **76**, 441–453.

566 McMillan, J. M., A. E. Hay, R. G. Lueck, and F. Wolk, 2016: Rates of dissipation of turbulent ki-
567 netic energy in a high reynolds number tidal channel. *Journal of Atmospheric and Oceanic Tech-*
568 *nology*, **33** (4), 817–837, doi:10.1175/JTECH-D-15-0167.1, URL [http://dx.doi.org/10.1175/](http://dx.doi.org/10.1175/JTECH-D-15-0167.1)
569 [JTECH-D-15-0167.1](http://dx.doi.org/10.1175/JTECH-D-15-0167.1), <http://dx.doi.org/10.1175/JTECH-D-15-0167.1>.

570 MicroStrain, I., 2010: Technical note: Coning and sculling. Tech. Rep. I0019, MicroStrain. URL
571 http://files.microstrain.com/TN-I0019_3DM-GX3-25__Coning_And_Sculling.pdf.

572 MicroStrain, I., 2012: *3DM-GX3-15,-25 MIP Data Communications Protocol*. URL [http:](http://files.microstrain.com/3DM-GX3-15-25-MIP-Data-Communications-Protocol.pdf)
573 [//files.microstrain.com/3DM-GX3-15-25-MIP-Data-Communications-Protocol.pdf](http://files.microstrain.com/3DM-GX3-15-25-MIP-Data-Communications-Protocol.pdf), retrieved
574 January 2014.

575 Miller, S. D., T. S. Hristov, J. B. Edson, and C. A. Friehe, 2008: Platform motion effects on
576 measurements of turbulence and air-sea exchange over the open ocean. *Journal of Atmospheric*

577 *and Oceanic Technology*, **25** (9), 1683–1694, doi:10.1175/2008JTECHO547.1, URL [http://dx.](http://dx.doi.org/10.1175/2008JTECHO547.1)
578 [doi.org/10.1175/2008JTECHO547.1](http://dx.doi.org/10.1175/2008JTECHO547.1), <http://dx.doi.org/10.1175/2008JTECHO547.1>.

579 Morison, J. R., J. W. Johnson, and S. A. Schaaf, 1950: The force exerted by surface waves on
580 piles. *Journal of Petroleum Technology*, **2** (05), 149–154.

581 Moum, J., and J. Nash, 2009: Mixing measurements on an equatorial ocean mooring. *Journal of*
582 *Atmospheric and Oceanic Technology*, **26** (2), 317–336.

583 Mücke, T., D. Kleinhans, and J. Peinke, 2011: Atmospheric turbulence and its influence on the
584 alternating loads on wind turbines. *Wind Energy*, **14**, 301–316.

585 Nash, J. D., L. F. Kilcher, and J. N. Moum, 2009: Structure and composition of a strongly
586 stratified, tidally pulsed river plume. *Journal of Geophysical Research*, **114**, C00B12, doi:
587 10.1029/2008JC005036.

588 Nash, J. D., E. Kunze, J. M. Toole, and R. W. Schmitt, 2004: Internal tide reflection
589 and turbulent mixing on the continental slope. *Journal of Physical Oceanography*,
590 **34** (5), 1117–1134, doi:10.1175/1520-0485(2004)034<1117:ITRATM>2.0.CO;2, URL [http://](http://dx.doi.org/10.1175/1520-0485(2004)034<1117:ITRATM>2.0.CO;2)
591 [dx.doi.org/10.1175/1520-0485\(2004\)034<1117:ITRATM>2.0.CO;2](http://dx.doi.org/10.1175/1520-0485(2004)034<1117:ITRATM>2.0.CO;2), [http://dx.doi.org/10.1175/](http://dx.doi.org/10.1175/1520-0485(2004)034<1117:ITRATM>2.0.CO;2)
592 [1520-0485\(2004\)034<1117:ITRATM>2.0.CO;2](http://dx.doi.org/10.1175/1520-0485(2004)034<1117:ITRATM>2.0.CO;2).

593 Nortek, 2005: *Vector Current Meter User Manual*. Vangkroken 2, NO-1351 RUD, Norway, h ed.

594 oáo Luis Marins, J., X. Yun, E. R. Bachmann, R. B. McGhee, and M. J. Zyda, 2001: An extended
595 Kalman filter for quaternion-based orientation estimation using MARG sensors. *International*
596 *conference on intelligent robots and systems*.

597 Paskyabi, M. B., and I. Fer, 2013: Turbulence measurements in shallow water from
598 a subsurface moored moving platform. *Energy Procedia*, **35**, 307 – 316, doi:[http://dx.](http://dx.doi.org/10.1016/j.egypro.2013.05.001)

doi.org/10.1016/j.egypro.2013.07.183, URL <http://www.sciencedirect.com/science/article/pii/S1876610213012691>.

Rippeth, T. P., E. Williams, and J. H. Simpson, 2002: Reynolds stress and turbulent energy production in a tidal channel. *Journal of Physical Oceanography*, **32**, 1242–1251, doi: 10.1175/1520-0485(2002)032<1242:RSATEP>2.0.CO;2.

Sreenivasan, K. R., 1995: On the universality of the Kolmogorov constant. *Physics of Fluids*, **7**, 2778–2784.

Stacey, M. T., S. G. Monismith, and J. R. Burau, 1999a: Measurements of reynolds stress profiles in unstratified tidal flow. *J. Geophys. Res.*, **104 (C5)**, 10 933–10 949, URL <http://dx.doi.org/10.1029/1998JC900095>.

Stacey, M. T., S. G. Monismith, and J. R. Burau, 1999b: Observations of turbulence in a partially stratified estuary. *Journal of Physical Oceanography*, **29**, 1950–1970.

Thomson, J., B. Polagye, V. Durgesh, and M. Richmond, 2012: Measurements of turbulence at two tidal energy sites in Puget Sound, WA. *Journal of Oceanic Engineering*, **37 (3)**, 363–374, doi:10.1109/JOE.2012.2191656.

Trowbridge, J. H., 1992: A simple description of the deepening and structure of a stably stratified flow driven by a surface stress. *Journal of Geophysical Research*, **97**, 15 529–15 543.

Trowbridge, J. H., W. R. Geyer, M. M. Bowen, and A. J. I. Williams, 1999: Near-bottom turbulence measurements in a partially mixed estuary: turbulent energy balance, velocity structure and along-channel momentum balance. *Journal of Physical Oceanography*, **29**, 3056–3072.

619 van der Walt, S., S. C. Colbert, and G. Varoquaux, 2011: The numpy array: A structure for efficient
620 numerical computation. *Computing in Science & Engineering*, **13**, 22–30, doi:10.1109/MCSE.
621 2011.37, URL <http://scitation.aip.org/content/aip/journal/cise/13/2/10.1109/MCSE.2011.37>.

622 VanZwieten, J. H., M. N. Egeland, K. D. von Ellenrieder, J. W. Lovenbury, and L. Kilcher, 2015:
623 Experimental evaluation of motion compensated adv measurements for in-stream hydrokinetic
624 applications. *Current, Waves and Turbulence Measurement (CWTM), 2015 IEEE/OES Eleventh*,
625 1–8, doi:10.1109/CWTM.2015.7098119.

626 Voulgaris, G., and J. H. Trowbridge, 1998: Evaluation of the acoustic doppler velocimeter (adv)
627 for turbulence measurements. *Journal of Atmospheric and Oceanic technology*, **15**, 272–289.

628 Walter, R. K., N. J. Nidzieko, and S. G. Monismith, 2011: Similarity scaling of turbulence spectra
629 and cospectra in a shallow tidal flow. *Journal of Geophysical Research: Oceans*, **116** (C10).

630 Wiles, P. J., T. P. Rippeth, J. H. Simpson, and P. J. Hendricks, 2006: A novel technique for
631 measuring the rate of turbulent dissipation in the marine environment. *Geophysical Research*
632 *Letters*, **33**, 21 608.

633 Winkel, D., M. Gregg, and T. Sanford, 1996: Resolving oceanic shear and velocity with the multi-
634 scale profiler. *Journal of Atmospheric and Oceanic Technology*, **13** (5), 1046–1072.

635 Wyngaard, J. C., L. Rockwell, and C. A. Friehe, 1985: Errors in the measurement of turbulence
636 upstream of an axisymmetric body. *Journal of Atmospheric and Oceanic Technology*, **2** (4),
637 605–614.

638 Zhang, Y., K. Streitlien, J. G. Bellingham, and A. B. Baggeroer, 2001: Acoustic
639 doppler velocimeter flow measurement from an autonomous underwater vehicle with
640 applications to deep ocean convection. *Journal of Atmospheric and Oceanic Tech-*

641 *nology*, **18** (12), 2038–2051, doi:10.1175/1520-0426(2001)018<2038:ADVFMF>2.0.CO;2,
642 URL [http://dx.doi.org/10.1175/1520-0426\(2001\)018<2038:ADVFMF>2.0.CO;2](http://dx.doi.org/10.1175/1520-0426(2001)018<2038:ADVFMF>2.0.CO;2), [http://dx.doi.](http://dx.doi.org/10.1175/1520-0426(2001)018<2038:ADVFMF>2.0.CO;2)
643 [org/10.1175/1520-0426\(2001\)018<2038:ADVFMF>2.0.CO;2](http://dx.doi.org/10.1175/1520-0426(2001)018<2038:ADVFMF>2.0.CO;2).

644	LIST OF FIGURES	
645	Fig. 1. Bathymetry of Admiralty Inlet at Admiralty Head.	35
646	Fig. 2. Schematic diagram of the TTM, not to scale.	36
647	Fig. 3. TTM components on the deck of the R/V Jack Robertson. The TTM includes two ADVs,	
648	with pressure-cases mounted on opposite sides of the fin. The anchor stack includes a pop-	
649	up buoy for retrieval. The green arrow indicates the vector from the IMU to the ADV head	
650	(face of the transmit transducer).	37
651	Fig. 4. Top: Alex DeKlerk checks to ensure that the StableMoor buoy is properly fastened to its	
652	anchor; the RDI workhorse ADCP can be seen in the rear instrument bay. A bridle is draped	
653	across the top of the buoy for deployment and recovery, and a small marker buoy fastened	
654	to the tail is useful during recovery. Middle: a close-up of the StableMoor in the ‘nose	
655	mode’ configuration shows the ADV head and the top of its pressure case. The green arrow	
656	indicates the vector from the IMU to the ADV head. Bottom: the StableMoor buoy in ‘wing	
657	mode’, floating on the ocean surface with the marker buoy trailing behind. The ADV heads	
658	mounted at the ends of the cross-beam are protruding above the waterline.	38
659	Fig. 5. The turbulence platform showing details of the ADV head and pressure case configuration.	
660	The green arrow indicates the vector from the IMU to the ADV head. The head-cable was	
661	taped out of the way beneath the sounding weight tail fins shortly after taking this photo.	39
662	Fig. 6. Spectra of \vec{u}_ω (yellow) and \vec{u}_a signals from the Microstrain IMU sitting on a motionless	
663	table. The \vec{u}_a signals are unfiltered (black), and high-pass filtered at 30s (magenta), 10s	
664	(blue), 5s (green). Vertical dotted lines indicate the filter frequency. The black horizontal	
665	dotted line indicates the noise-level of a Nortek Vector ADV configured to measure $\pm 4\text{m/s}$.	
666	The shaded region indicates the range of spectra presented herein ($0.002 < \text{tke} < 0.03 \text{ m}^2/\text{s}^2$,	
667	$1\text{e-}5 < \varepsilon < 5\text{e-}4 \text{ W/kg}$).	40
668	Fig. 7. Time series of tidal velocity at Admiralty Head from TTM measurements (black), and an	
669	acoustic Doppler profiler (red). The profiler measurements—taken at the same depth as the	
670	ADV on the TTM—were contaminated by acoustic reflection from the strongback fin when	
671	it was inline with one of the profiler’s beams. Note that the vertical scale on the three axes	
672	vary by more than an order of magnitude; the small ticks in A and B are equivalent to the	
673	ticks in C.	41
674	Fig. 8. Turbulence spectra from the June 2014 TTM deployment. Each column is for a range of	
675	streamwise velocity magnitudes (indicated at top). The rows are for each component of	
676	velocity (indicated to the lower-right of the right column). The uncorrected spectra are in	
677	black and the corrected spectra are blue, and the spectra of ADV head motion, \vec{u}_h , is red (also	
678	indicated in the legend). The vertical red dotted line indicates the filter frequency applied	
679	to the IMU accelerometers when estimating \vec{u}_h ; below this frequency $S\{\vec{u}_h\}$ is plotted as a	
680	dashed line. Diagonal black dotted lines indicate a $f^{-5/3}$ slope. The number of spectral-	
681	ensembles, N, in each column is indicated in the top row.	42
682	Fig. 9. Turbulence spectra from the StableMoor buoy. The axes-layout and annotations are iden-	
683	tical to Figure 8, except that $S\{\vec{u}_h\}$ is plotted as a solid line at all frequencies because it is	
684	measured at all frequencies.	43
685	Fig. 10. Turbulence spectra from the turbulence torpedo during a 35 minute period when the mean	
686	velocity was 1.3 m/s. Annotations and line colors are identical to Figure 8.	44

687	Fig. 11.	The real part of the cross-spectral density between velocity components measured by the	
688		TTM. The upper-row is the u - v cross-spectral density, the middle-row is the u - w cross-	
689		spectral density, and the bottom-row is the v - w cross-spectral density. The columns are for	
690		different ranges of the stream-wise mean velocity magnitude (indicated above the top row).	
691		The blue line is the cross-spectrum between components of motion-corrected velocity, the	
692		red line is the cross-spectrum between components of head-motion, and the black line is	
693		the cross-spectrum between components of uncorrected velocity. The light-blue shading	
694		indicates one standard deviation of the C for the motion corrected cross-spectral density. N	
695		is the number of spectral ensembles in each column. The number in the lower right corner	
696		of each panel is the motion-corrected Reynold's stress (integral of the blue line) in units of	
697		$1\text{e-4 m}^2\text{s}^{-2}$	45
698	Fig. 12.	Time-series of mean velocities (A), turbulence energy and its components (B), Reynold's	
699		stresses (C), and turbulence dissipation rate (D) measured by the TTM during the June,	
700		2014 deployment. Shading indicates periods of ebb ($\bar{u} > 1.0$, grey), and flood ($\bar{u} < -1.0$,	
701		lighter grey).	46
702	Fig. 13.	$P_{u\bar{z}}$ vs. ε during the June 2014 TTM deployment for values of $ u > 1$ m/s. Values of	
703		'negative' production are indicated as open circles.	47
704	Fig. 14.	A log-log plot of ε versus \bar{U} for the June 2014 TTM (diamonds) and May 2015 StableMoor	
705		(dots) deployments, during ebb (left) and flood (right). Black points are 5 minute averages.	
706		Green dots are mean values within speed bins of 0.2 m s^{-1} width that have at least 10 points	
707		(50 minutes of data); their vertical bars are 95% bootstrap confidence intervals. The blue	
708		line shows a U^3 slope, where the proportionality constant (blue box) is calculated by taking	
709		the log-space mean of ε/U^3	48
710	Fig. 15.	Coherence between IMU-measured motion of StableMoor buoy and ADP bottom track ve-	
711		locity for $1.0 < \bar{U} < 1.5$. The vertical dotted line indicates the 95% confidence level for the	
712		102 spectral windows in this estimate.	49

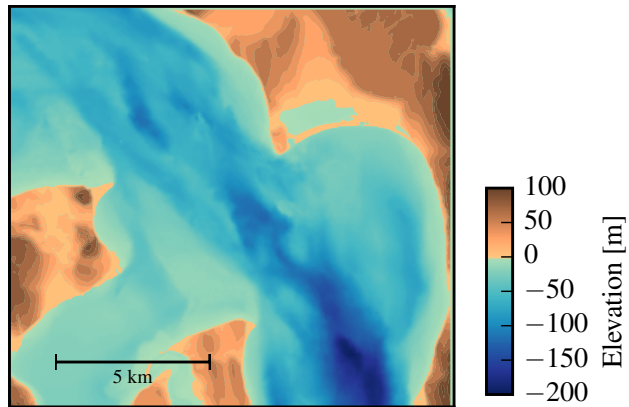


FIG. 1. Bathymetry of Admiralty Inlet at Admiralty Head.

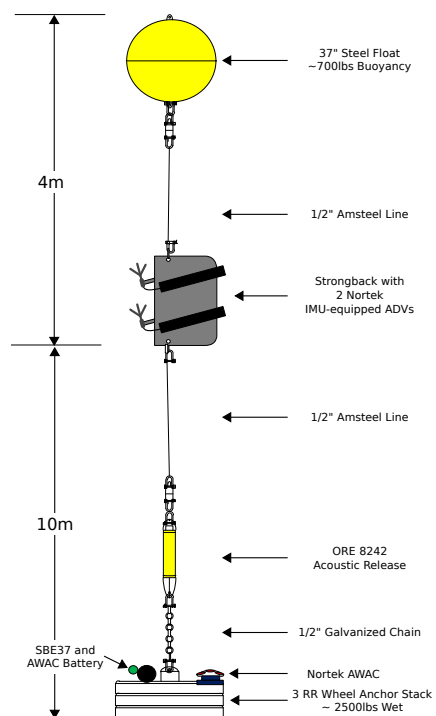


FIG. 2. Schematic diagram of the TTM, not to scale.



713 FIG. 3. TTM components on the deck of the R/V Jack Robertson. The TTM includes two ADVs, with
 714 pressure-cases mounted on opposite sides of the fin. The anchor stack includes a pop-up buoy for retrieval. The
 715 green arrow indicates the vector from the IMU to the ADV head (face of the transmit transducer).



716 FIG. 4. Top: Alex DeKlerk checks to ensure that the StableMoor buoy is properly fastened to its anchor; the
 717 RDI workhorse ADCP can be seen in the rear instrument bay. A bridle is draped across the top of the buoy
 718 for deployment and recovery, and a small marker buoy fastened to the tail is useful during recovery. Middle: a
 719 close-up of the StableMoor in the ‘nose mode’ configuration shows the ADV head and the top of its pressure
 720 case. The green arrow indicates the vector from the IMU to the ADV head. Bottom: the StableMoor buoy in
 721 ‘wing mode’, floating on the ocean surface with the marker buoy trailing behind. The ADV heads mounted at
 722 the ends of the cross-beam are protruding above the waterline.



723 FIG. 5. The turbulence platform showing details of the ADV head and pressure case configuration. The green
724 arrow indicates the vector from the IMU to the ADV head. The head-cable was taped out of the way beneath the
725 sounding weight tail fins shortly after taking this photo.

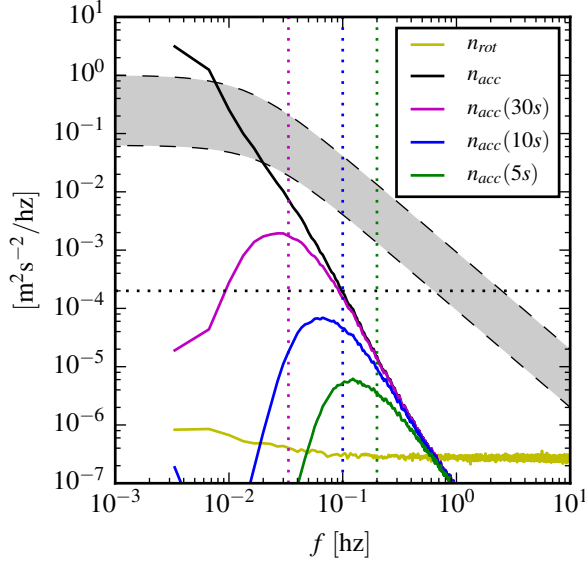
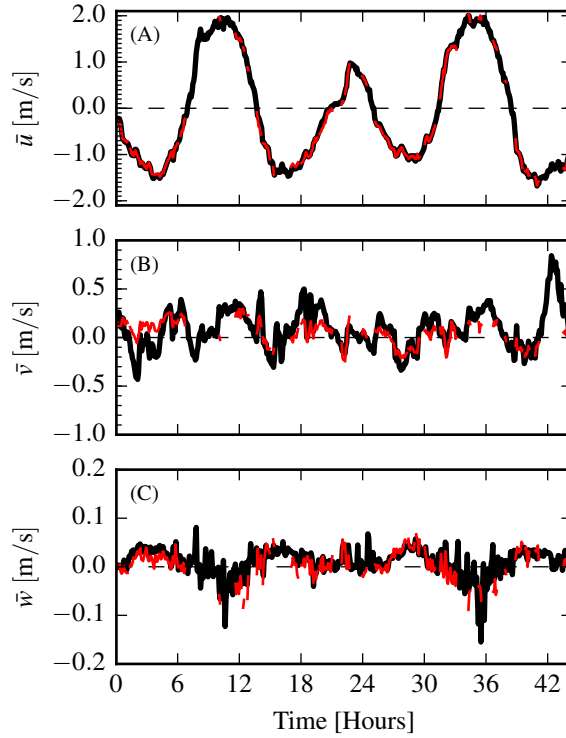


FIG. 6. Spectra of \vec{u}_ω (yellow) and \vec{u}_a signals from the Microstrain IMU sitting on a motionless table. The \vec{u}_a signals are unfiltered (black), and high-pass filtered at 30s (magenta), 10s (blue), 5s (green). Vertical dotted lines indicate the filter frequency. The black horizontal dotted line indicates the noise-level of a Nortek Vector ADV configured to measure $\pm 4\text{m/s}$. The shaded region indicates the range of spectra presented herein ($0.002 < \text{tke} < 0.03 \text{ m}^2/\text{s}^2$, $1\text{e-}5 < \varepsilon < 5\text{e-}4 \text{ W/kg}$).



731 FIG. 7. Time series of tidal velocity at Admiralty Head from TTM measurements (black), and an acoustic
 732 Doppler profiler (red). The profiler measurements—taken at the same depth as the ADV on the TTM—were
 733 contaminated by acoustic reflection from the strongback fin when it was inline with one of the profiler’s beams.
 734 Note that the vertical scale on the three axes vary by more than an order of magnitude; the small ticks in A and
 735 B are equivalent to the ticks in C.

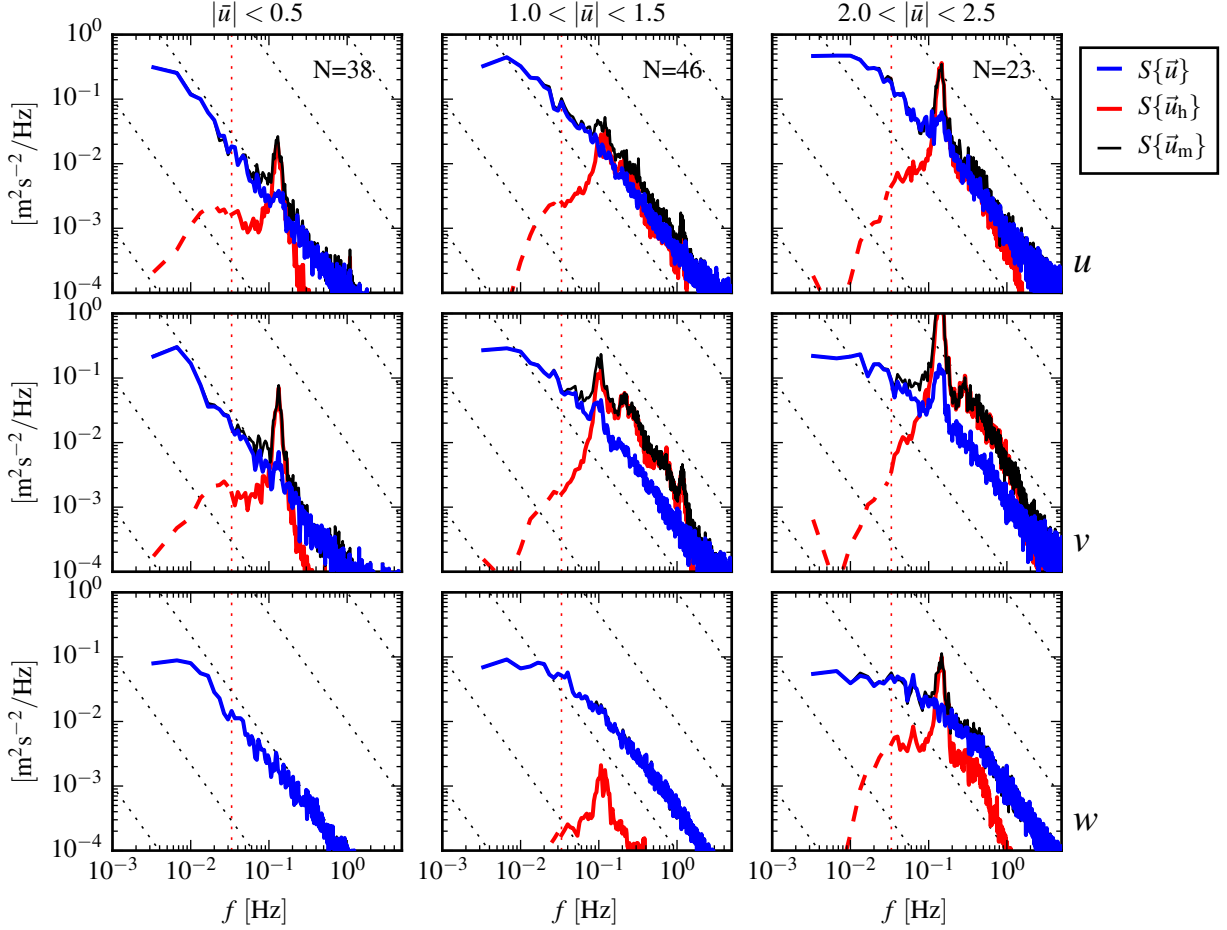


FIG. 8. Turbulence spectra from the June 2014 TTM deployment. Each column is for a range of streamwise velocity magnitudes (indicated at top). The rows are for each component of velocity (indicated to the lower-right of the right column). The uncorrected spectra are in black and the corrected spectra are blue, and the spectra of ADV head motion, \vec{u}_h , is red (also indicated in the legend). The vertical red dotted line indicates the filter frequency applied to the IMU accelerometers when estimating \vec{u}_h ; below this frequency $S\{\vec{u}_h\}$ is plotted as a dashed line. Diagonal black dotted lines indicate a $f^{-5/3}$ slope. The number of spectral-ensembles, N , in each column is indicated in the top row.

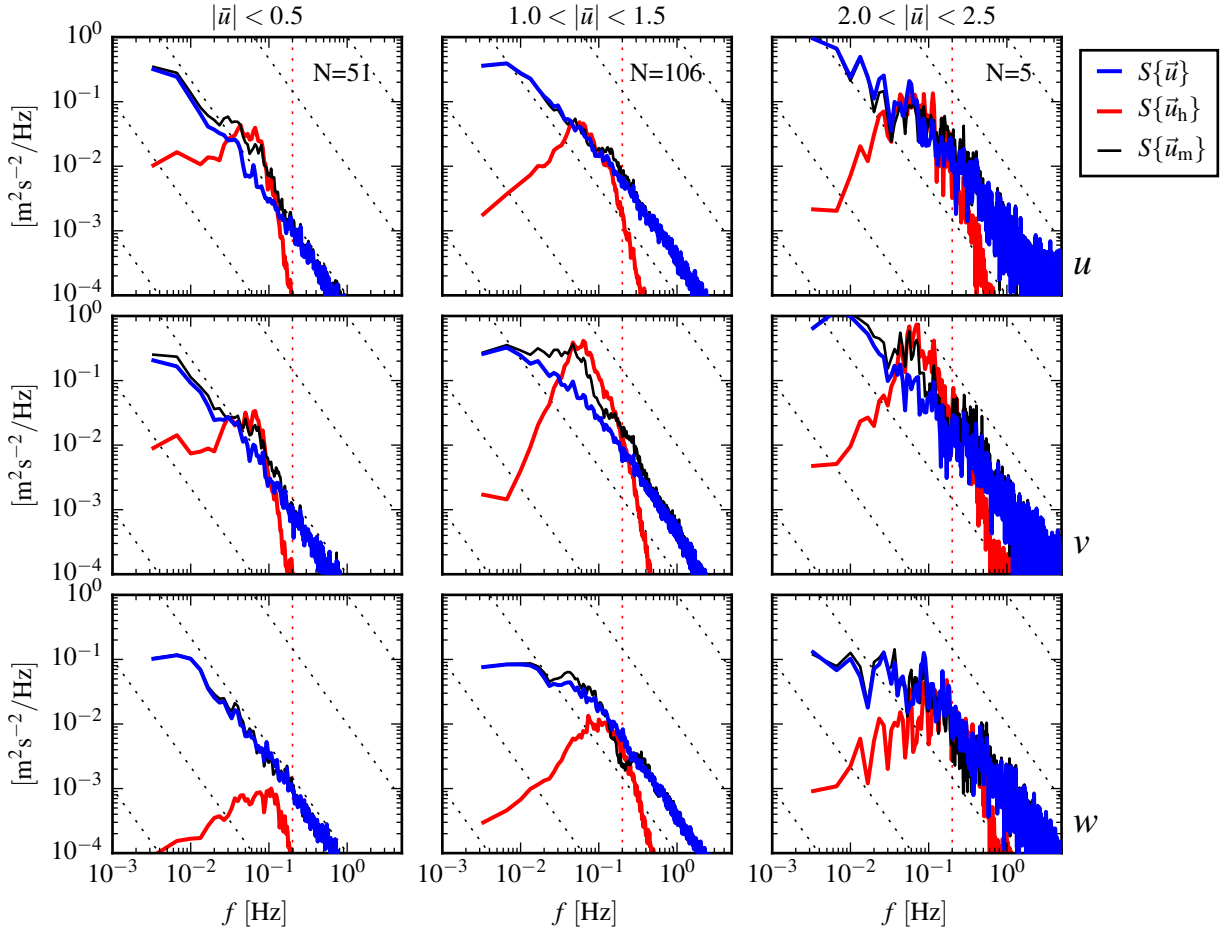
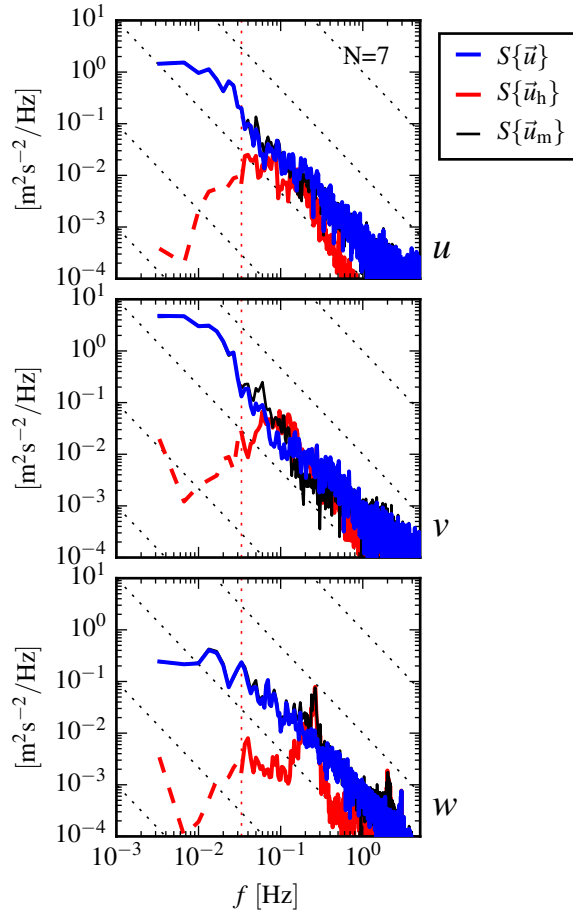


FIG. 9. Turbulence spectra from the StableMoor buoy. The axes-layout and annotations are identical to Figure 8, except that $S\{\vec{u}_h\}$ is plotted as a solid line at all frequencies because it is measured at all frequencies.



745 FIG. 10. Turbulence spectra from the turbulence torpedo during a 35 minute period when the mean velocity
 746 was 1.3 m/s. Annotations and line colors are identical to Figure 8.

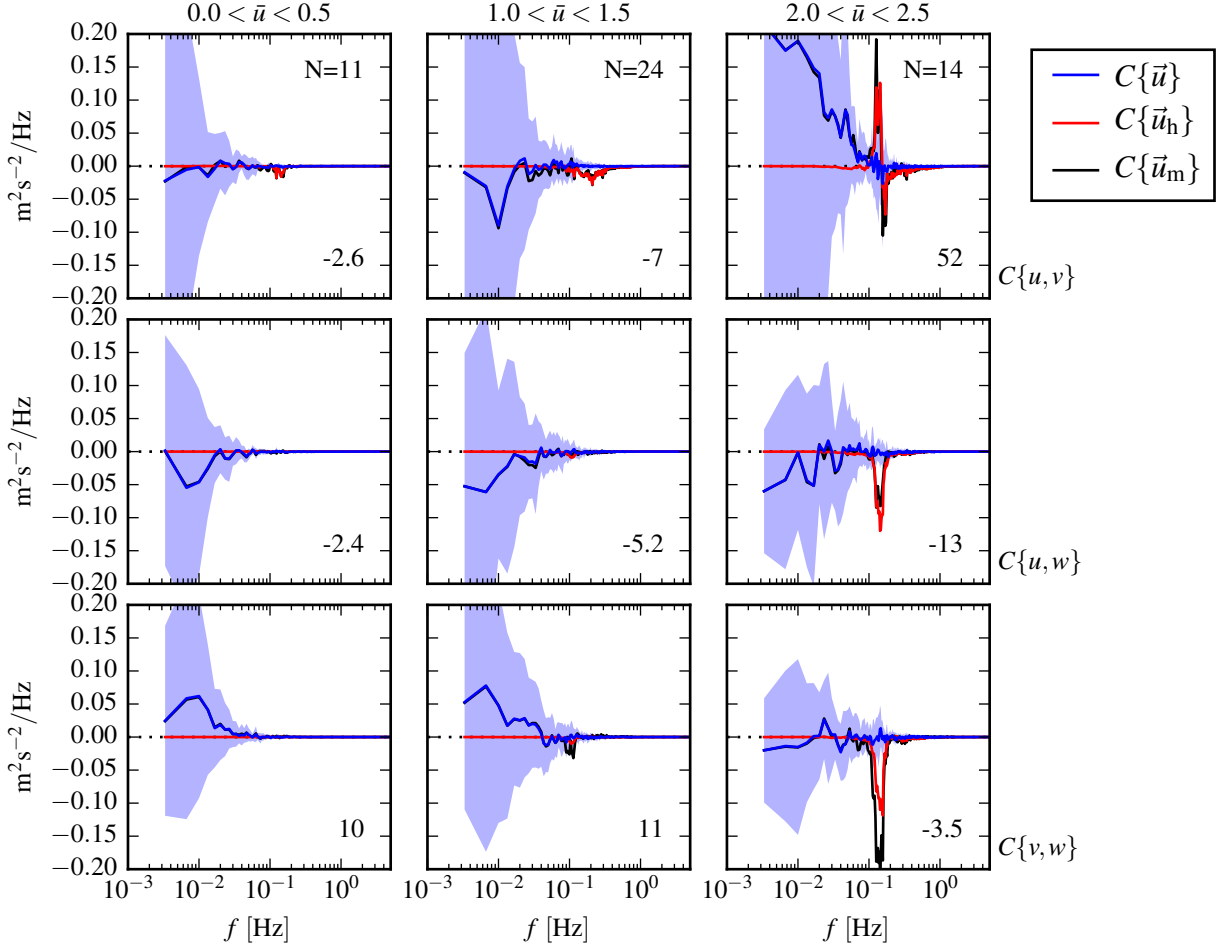


FIG. 11. The real part of the cross-spectral density between velocity components measured by the TTM. The upper-row is the u - v cross-spectral density, the middle-row is the u - w cross-spectral density, and the bottom-row is the v - w cross-spectral density. The columns are for different ranges of the stream-wise mean velocity magnitude (indicated above the top row). The blue line is the cross-spectrum between components of motion-corrected velocity, the red line is the cross-spectrum between components of head-motion, and the black line is the cross-spectrum between components of uncorrected velocity. The light-blue shading indicates one standard deviation of the C for the motion corrected cross-spectral density. N is the number of spectral ensembles in each column. The number in the lower right corner of each panel is the motion-corrected Reynold's stress (integral of the blue line) in units of $1\text{e-}4 \text{ m}^2\text{s}^{-2}$.

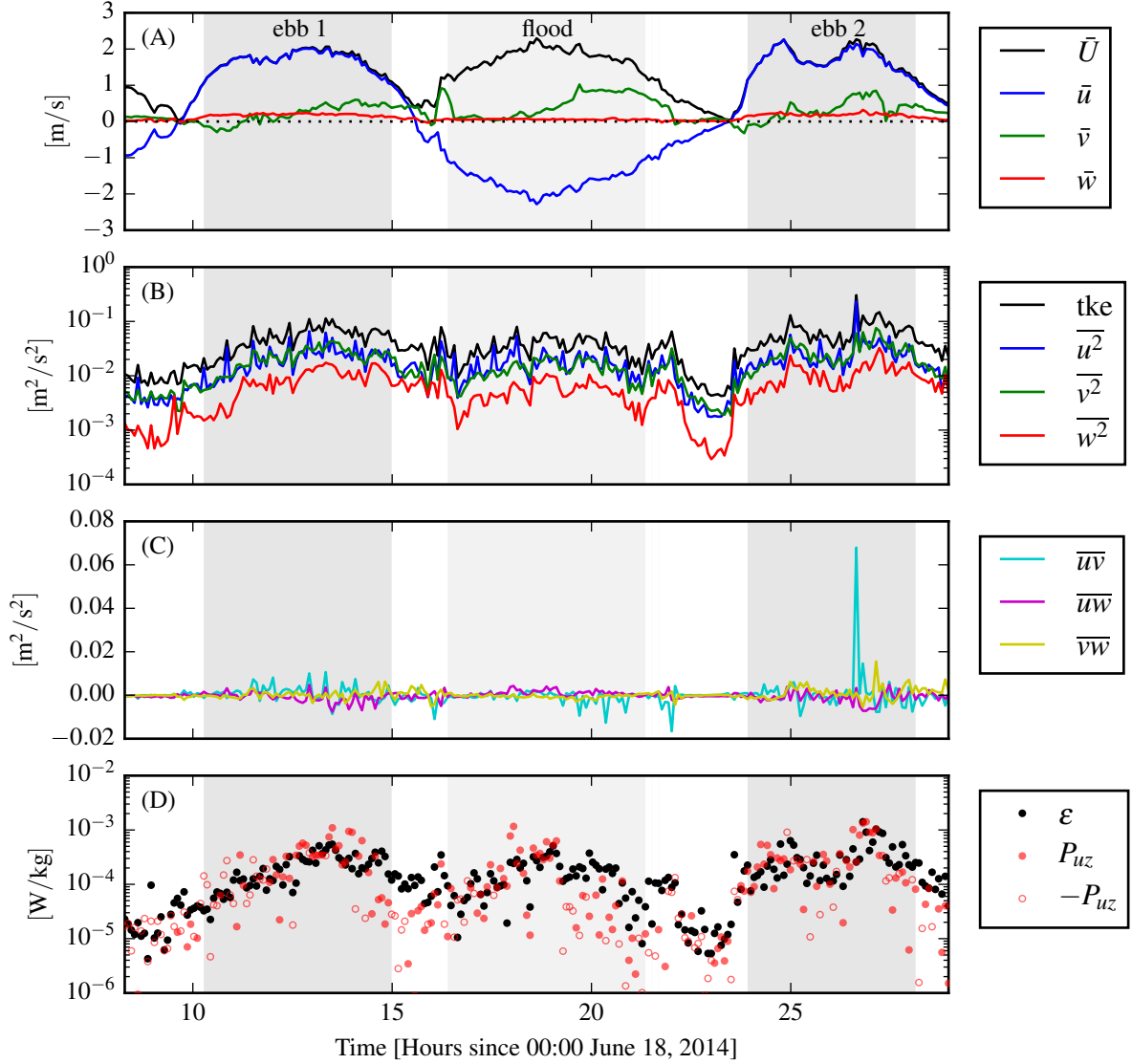


FIG. 12. Time-series of mean velocities (A), turbulence energy and its components (B), Reynold's stresses (C), and turbulence dissipation rate (D) measured by the TTM during the June, 2014 deployment. Shading indicates periods of ebb ($\bar{u} > 1.0$, grey), and flood ($\bar{u} < -1.0$, lighter grey).

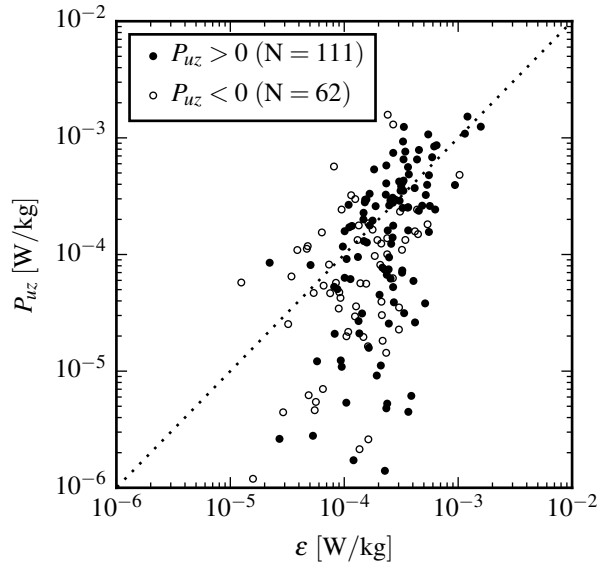


FIG. 13. P_{uz} vs. ε during the June 2014 TTM deployment for values of $|u| > 1$ m/s. Values of ‘negative’
production are indicated as open circles.

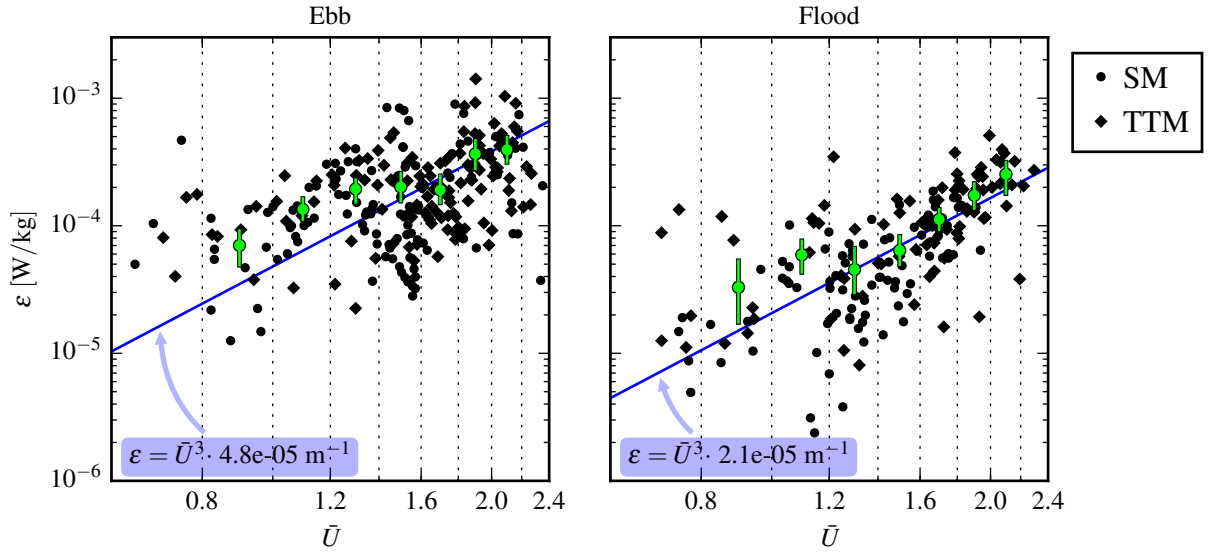


FIG. 14. A log-log plot of ε versus \bar{U} for the June 2014 TTM (diamonds) and May 2015 StableMoor (dots) deployments, during ebb (left) and flood (right). Black points are 5 minute averages. Green dots are mean values within speed bins of 0.2 m s^{-1} width that have at least 10 points (50 minutes of data); their vertical bars are 95% bootstrap confidence intervals. The blue line shows a U^3 slope, where the proportionality constant (blue box) is calculated by taking the log-space mean of ε/U^3 .

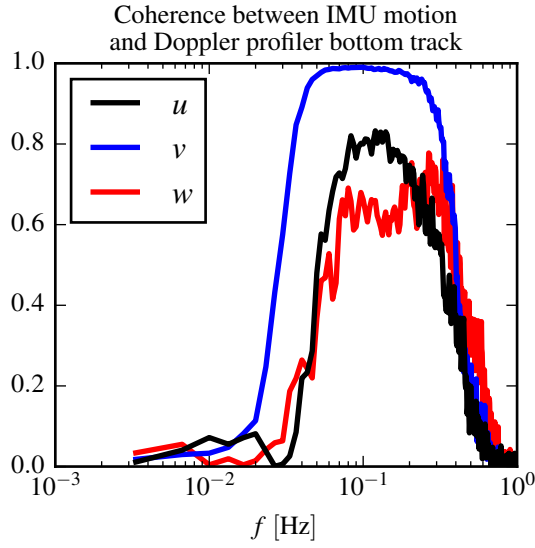


FIG. 15. Coherence between IMU-measured motion of StableMoor buoy and ADP bottom track velocity for $1.0 < \bar{U} < 1.5$. The vertical dotted line indicates the 95% confidence level for the 102 spectral windows in this estimate.